Atmospheric Environment 54 (2012) 557–567

Contents lists available at SciVerse ScienceDirect

Atmospheric Environment

journal homepage: www.elsevier.com/locate/atmosenv

Potential of the International Monitoring System radionuclide network for inverse modelling

Mohammad Reza Koohkan [a,b], Marc Bocquet [a,b,*], Lin Wu [a,b], Monika Krysta [c]

[a] Université Paris-Est, CEREA, Joint laboratory École des Ponts ParisTech and EDF R&D, Champs-sur-Marne, France
[b] INRIA, Paris Rocquencourt Research Centre, France
[c] CTBTO, IDC, Vienna, Austria

ARTICLE INFO

Article history:
Received 7 July 2011
Received in revised form
6 February 2012
Accepted 9 February 2012

Keywords:
Inverse modelling
Atmospheric dispersion
Comprehensive Nuclear-Test-Ban Treaty
Radionuclides
Multiscale data assimilation
Network design

ABSTRACT

The International Monitoring System (IMS) radionuclide network enforces the Comprehensive Nuclear-Test-Ban Treaty which bans nuclear explosions. We have evaluated the potential of the IMS radionuclide network for inverse modelling of the source, whereas it is usually assessed by its detection capability. To do so, we have chosen the *degrees of freedom for the signal* (DFS), a well established criterion in remote sensing, in order to assess the performance of an inverse modelling system. Using a recent multiscale data assimilation technique, we have computed optimal adaptive grids of the source parameter space by maximising the DFS. This optimisation takes into account the monitoring network, the meteorology over one year (2009) and the relationship between the source parameters and the observations derived from the FLEXPART Lagrangian transport model. Areas of the domain where the grid-cells of the optimal adaptive grid are large emphasise zones where the retrieval is more uncertain, whereas areas where the grid-cells are smaller and denser stress regions where more source variables can be resolved.

The observability of the globe through inverse modelling is studied in strong, realistic and small model error cases. The strong error and realistic error cases yield heterogeneous adaptive grids, indicating that information does not propagate far from the monitoring stations, whereas in the small error case, the grid is much more homogeneous. In all cases, several specific continental regions remain poorly observed such as Africa as well as the tropics, because of the trade winds. The northern hemisphere is better observed through inverse modelling (more than 60% of the total DFS) mostly because it contains more IMS stations. This unbalance leads to a better performance of inverse modelling in the northern hemisphere winter. The methodology is also applied to the subnetwork composed of the stations of the IMS network which measure noble gases.

1. Introduction

1.1. The IMS network and the CTBT enforcement

The Comprehensive Nuclear-Test-Ban Treaty (CTBT) signed by 182 states bans nuclear explosions (United Nations, 1996). The monitoring of the treaty is implemented by the United Nations CTBT Organisation (CTBTO), based in Vienna, Austria. It operates an International Monitoring System (IMS) and collects seismic, infrasound, hydroacoustic data as well as radionuclide (particulate matter and noble gases) activity concentrations. This article focuses on the latter. Upon completion of the installation, the radionuclide IMS network will have 80 stations. As of June 2011, 60 stations are certified and operational. The instruments are radionuclide gamma detectors coupled to particle filters. Each station is capable to provide for highly sensitive gamma-ray spectroscopy of the airborne particulate material sampled in filters being exchanged once a day according to a known schedule. Depending on the radionuclide considered, detection limits of 30 μ Bq are achieved. Consequently, these stations allow to deliver 24 h-averaged activity concentrations for several particulate/aerosol species: caesium-137, caesium-134, iodine-131 (aerosol form), etc. In the long term, 40 of those stations will also be able to measure noble gases (xenon-131 m, xenon-133, xenon-133 m, xenon-135), among which 24 are operating as of June 2011.

The locations of 79 (among 80) stations are detailed in the treaty, even though the actual locations could slightly differ (see http://www.ctbto.org/map). The design of the network has been validated using dispersion modelling. For instance, using a global atmospheric transport model (ATM), one can compute the ability of

* Corresponding author. Université Paris-Est, CEREA, Joint laboratory École des Ponts ParisTech and EDF R&D, Champs-sur-Marne, France.
E-mail address: bocquet@cerea.enpc.fr (M. Bocquet).

1352-2310/$ – see front matter © 2012 Elsevier Ltd. All rights reserved.
doi:10.1016/j.atmosenv.2012.02.044

the monitoring network to detect a release stemming from any location on Earth (Hourdin and Issartel, 2000; Wotawa et al., 2003, 2010; Saey et al., 2007; Ringbom and Miley, 2009). Recently, the radionuclide IMS network has measured the Fukushima Daiichi plume throughout the world, although only part of the observations has been disclosed.

The observations of the IMS radionuclide network can be utilised to globally detect a nuclear test in any environment. This includes the capability to discriminate a clandestine nuclear test from any other kind of underground explosion. The radionuclide observations could also help to characterise a test (location, signature and intensity) using inverse modelling techniques. The objective of this article is to determine the potential of the IMS radionuclide network for inverse modelling of the source term, using rigorous mathematical tools in conjunction with global or regional ATMs.

1.2. Inverse modelling of tracers

The application of inverse modelling techniques to the reconstruction of the source term is recent in atmospheric dispersion. The European Tracer Experiment (ETEX, Nodop et al. (1998)), initially triggered by the Chernobyl accident, served as a playground to test inverse methodologies (Robertson and Langner, 1998; Pudykiewicz, 1998; Seibert and Stohl, 2000; Issartel and Baverel, 2003; Bocquet, 2005a, b). Full reconstructions using real data with results close to the known characteristics of the source have been obtained (Bocquet, 2007; Krysta et al., 2008). These authors used methodologies inspired by geophysical data assimilation techniques: the field to retrieve is discretised into a spatially organised large set of source variables/parameters. Alternatively, the so-called *parametric* methods rely on the optimisation of a restricted set of variables that parametrise the source term. In the specific case of accidental dispersion, the lat-lon coordinates and the emission rate parametrise the source (Delle Monache et al., 2008; Yee et al., 2008).

As far as real radionuclide dispersion events are concerned, these methodologies have been tested on the Algeciras dispersion event (Krysta and Bocquet, 2007; Delle Monache et al., 2008), with about hundred caesium-137 integrated activity concentration measurements. The results are satisfying but mostly because of the very simple shape of the source (a single peak). The inverse modelling approach was also applied to the atmospheric source term of Chernobyl (caesium-137, caesium-134, and iodine-131) by Davoine and Bocquet (2007); Bocquet (in press) with an estimation of the source terms consistent with the official unscear source term (United Nations, 2000). Reconstruction of the source term was also performed for a North Korea nuclear test measured by the IMS radionuclide network (Becker et al., 2010), although the reconstruction was based on another type of inverse modelling method. More recently Winiarek et al. (2012); Stohl et al. (2011) have used inverse modelling to estimate the Fukushima Daiichi atmospheric source terms for caesium-137 and iodine-131 in the first reference and caesium-137 and xenon-133 in the second reference. Among other sources of data, these studies used activity concentrations from the IMS network.

In this context, the inverse modelling approach remains a difficult one, because:

- the observations are ground-based and local. Activity concentration measurements are sparse, infrequent or integrated, as opposed to gamma dose measurements. Moreover, point-wise observations may lead to representativeness errors, with a magnitude that depends on whether the dispersion model is Eulerian or Lagrangian.
- The dispersion models remain imprecise. They are driven by meteorological fields of increasing precision and reliability at a given resolution, but the planetary boundary layer remains difficult to model, and the vertical turbulent diffusion is still uncertain. With only a few documented field experiments, the microphysical properties of the radionuclides in the atmosphere, are still difficult to grasp. Therefore the physical parametrisations implemented in the ATMs (dry deposition, wet scavenging, aerosol modelling, granulometry of particles) remain gross.

Beyond its own interest, inverse modelling of the source term is also the *sine qua non* condition for a proper forecasting of the resulting plume, as was illustrated by Politis and Robertson (2004); Bocquet (2007); Abida and Bocquet (2009).

1.3. Objectives and outline

Detectability has been used to assess the performance of the IMS radionuclide network (Hourdin and Issartel, 2000; Wotawa et al., 2003, 2010; Ringbom and Miley, 2009). A more complex criterion is a measure of the ability to interpolate activity concentrations in between the stations of the network, using geostatistical techniques (Wu and Bocquet (2011) and references therein). It has been used to assess and even design a radionuclide monitoring network (Abida et al., 2008). One step further in complexity, our goal is to evaluate the potential of the IMS radionuclide network for inverse modelling, using an objective quantitative criterion: the degrees of freedom for the signal.

In Section 2, we define the typical inverse modelling experiment that could serve the CTBT enforcement. The average quality of an inversion is rigorously defined by the degrees of freedom for the signal. We do not focus on the particular results of specific inverse modelling experiments. This was done for instance by Winiarek et al. (2011) in the same context. Instead, we focus on the average ability of inverse modelling to extract information from the measurements. A multiscale formalism is used to rigorously diagnose how the information contained in the observations should optimally be spread in regions of the world. In Section 3, the formalism is applied to the IMS radionuclide network using all influence functions of year 2009 computed by CTBTO that archives and disseminates them as so-called source-receptor sensitivity (SRS) fields. Adaptive grids that maximise the degrees of freedom for the signal are computed. By construction, they are optimal for the assimilation of observations. For a given number of grid-cells, they are numerically more efficient, and bear less aggregation errors (representativeness errors from the observation perspective) than regular grids with the same number of grid-cells. They rigorously determine the ability of the monitoring network to resolve source variables through data assimilation. Consequently, they allow to pinpoint well observed (from inverse modelling) as well as poorly observed regions of the world. They have indirect implications on the way to optimise the design of the network. The technique is also applied to the subnetwork of the stations that monitor noble gases. The difference between an Eulerian and a Lagrangian model in the design of those adaptive grids is examined, using a specific region of the globe. Conclusions are given in Section 4.

2. Methodology of data assimilation

2.1. Inverse modelling with Gaussian statistical assumptions

The source parameters are the unknown variables. Each one of them is attached to a grid-cell in a domain Ω, and to a time interval. At first, Ω will be the globe. At the end of Section 3, Ω will be a limited area of the globe. We assume that the domain Ω is discretised. We shall use unprojected (lat-lon) coordinates in the

following, with N_x meridians and $N_y - 1$ parallels. The source vector $\boldsymbol{\sigma}$ is defined on this grid. It has an extension in time of N_t time-steps, so that $\boldsymbol{\sigma}$ is a vector of dimension $N_x N_y N_t$. The radionuclide plume is observed by the monitoring network. The observations yield a measurement vector $\boldsymbol{\mu}$ in $\mathbb{R}^d$.

The partial differential equations that rule the physics of dispersion are usually the result of simple modelling that leads to linearity in the concentrations. Transport and physical processes, such as advection, diffusion, radioactive decay, dry deposition, and wet scavenging, can be modelled as linear processes in the concentrations. However it should be kept in mind that this is an approximation, that rules out aging of noble gases that may migrate to the aerosol phase, or complex wet scavenging and dry deposition parametrisations.

With this linearity, and in the absence of boundary conditions, or using clean air boundary conditions which are suitable for accidental release, a source–receptor relationship between the observation vector $\boldsymbol{\mu}$ and the source $\boldsymbol{\sigma}$ is established. It is formalised by the Jacobian matrix $\mathbf{H}$.

$$\boldsymbol{\mu} = \mathbf{H}\boldsymbol{\sigma} + \boldsymbol{\epsilon}, \tag{1}$$

where the vector $\boldsymbol{\epsilon}$ represents errors of all kinds: instrumental error, representativeness error, and model errors.

The simplest approach for non-parametric inverse modelling is to minimise the discrepancy

$$\mathscr{L}(\boldsymbol{\sigma}) = \frac{1}{2}(\boldsymbol{\mu} - \mathbf{H}\boldsymbol{\sigma})^{\mathrm{T}}\mathbf{R}^{-1}(\boldsymbol{\mu} - \mathbf{H}\boldsymbol{\sigma}), \tag{2}$$

where $\mathbf{R} = \mathrm{E}[\boldsymbol{\epsilon}\boldsymbol{\epsilon}^{\mathrm{T}}]$ is the observation error covariance matrix, which, in this ground observation context, is almost always assumed diagonal, even though transport model errors could induce some cross-correlations. Following the Bayesian paradigm of geophysical data assimilation, a background term (also called regularisation term in this inverse modelling context) should be added to the cost function Eq. (2). This term is obviously unavoidable when the number of variables to retrieve is greater than the number of observations. However, even with a larger set of observations, a regularisation may be needed because of the errors that impoverish the information content of the observations, and because of the lack of observability of some regions of the source space. It is often said that these inverse problems are ill-posed.

It was shown in Winiarek et al. (2011), that even when the location of the source is well known (anticipated in the case of Fukushima Daiichi, or with delay in the case of the Chernobyl) so that only a temporal rate profile should be retrieved, and even when the observations are abundant, a background term is still necessary in a significant fraction of the cases. In the case of Chernobyl, where the location is supposed to be known in re-analysis, Bocquet (in press) has demonstrated that a problem without a properly defined background but with much more observations than source parameters can lead to aberrant total retrieved activity for the source term.

Therefore, it is often safer to use the objective function with a regularisation term:

$$\mathscr{L}(\boldsymbol{\sigma}) = \frac{1}{2}(\boldsymbol{\mu} - \mathbf{H}\boldsymbol{\sigma})^{\mathrm{T}}\mathbf{R}^{-1}(\boldsymbol{\mu} - \mathbf{H}\boldsymbol{\sigma}) + \frac{1}{2}(\boldsymbol{\sigma} - \boldsymbol{\sigma}_b)^{\mathrm{T}}\mathbf{B}^{-1}(\boldsymbol{\sigma} - \boldsymbol{\sigma}_b), \tag{3}$$

where $\boldsymbol{\sigma}_b$ is the first guess (or background), an estimation of the source before the observations are assimilated, and $\mathbf{B}$ is the background error covariance matrix. In the context of an accidental release, it is reasonable to assume $\boldsymbol{\sigma}_b = 0$ for the accidental source, since so little is known about it. In the case of noble gases, there could be significant diffuse natural (radon) or anthropogenic (xenon) emissions, that would have to be taken into account through an offset term in Eq. (1), or incorporated into the inverse modelling scheme. In that latter case, a non-zero diffuse background $\boldsymbol{\sigma}_b$ would be defined from their emission inventories.

Matrix $\mathbf{B}$ is a rather well studied object in meteorological and oceanographical data assimilation, even though its modelling is complex. In our context, $\mathbf{B}$ is very poorly known, since it is meant to measure our ignorance on the source term before the accident or the nuclear test, which is difficult to quantify. The $\mathbf{B}$ matrix related to noble gas with an estimated background which measures the errors in the inventory, may be better known. In the following, we are not considering such non-trivial background, and we will focus on the accidental release part. However the formalism used in this article can cope with more complex situations.

A posteriori parameter estimation techniques, such as L-curve, maximum-likelihood, generalised cross-validation (Vogel, 2002; Hansen, 2010), can efficiently help to assess the background term in an accidental context (Davoine and Bocquet, 2007; Krysta et al., 2008; Saide et al., 2011; Winiarek et al., 2012), where a single realisation of the set of observations is available (as opposed to routine pollution). However it should be clear that the errors represented by $\mathbf{R}$ and $\mathbf{B}$ are very difficult to assess in this context.

In the absence of any constraint such as the positivity of $\boldsymbol{\sigma}$, the best linear unbiased estimator of the source is given by the argument of the minimum of Eq. (3)

$$\boldsymbol{\sigma}_a = \boldsymbol{\sigma}_b + \mathbf{B}\mathbf{H}^{\mathrm{T}}\left(\mathbf{R} + \mathbf{H}\mathbf{B}\mathbf{H}^{\mathrm{T}}\right)^{-1}(\boldsymbol{\mu} - \mathbf{H}\boldsymbol{\sigma}_b). \tag{4}$$

The uncertainty of this estimator is given by the analysis error covariance matrix

$$\mathbf{P}_a = \left(\mathbf{B}^{-1} + \mathbf{H}^{\mathrm{T}}\mathbf{R}^{-1}\mathbf{H}\right)^{-1}. \tag{5}$$

which is obtained as the inverse matrix of the Hessian of Eq. (3), which represents the precision matrix of the estimator. It is often equivalently rewritten as

$$\mathbf{P}_a = \mathbf{B} - \mathbf{B}\mathbf{H}^{\mathrm{T}}\left(\mathbf{R} + \mathbf{H}\mathbf{B}\mathbf{H}^{\mathrm{T}}\right)^{-1}\mathbf{H}\mathbf{B}, \tag{6}$$

which is to be used later.

More advanced methodologies that are able to handle the non-Gaussianity of errors, can lead to more sophisticated estimators of the a posteriori errors (see Bocquet et al. (2010) and references therein). However, second-order moments of the error distribution still provide an approximation of the posterior error statistics. In this case, $\mathbf{P}_a$ is approximately obtained as the inverse of the Hessian of the cost function,

2.2. Information content and DFS

After the analysis, a scalar residual posterior uncertainty is given by $\mathrm{Tr}(\mathbf{P}_a)$. The reduction of uncertainty in the data assimilation process can be measured by a related quantity: $\mathrm{Tr}(\mathbf{I}_N - \mathbf{P}_a\mathbf{B}^{-1})$, which identifies with the *degrees of freedom for the signal*, abbreviated DFS in the following (Rodgers, 2000). The DFS are often used in the inversion of satellite-based instrument radiances. In our context, it measures the fractional number of observations that are effectively used in the inversion to retrieve the source. Explicitly, one has

$$\mathscr{I}_{\mathrm{DFS}} = \mathrm{Tr}(\mathbf{I}_N - \mathbf{P}_a\mathbf{B}^{-1}) = \mathrm{Tr}\left(\mathbf{B}\mathbf{H}^{\mathrm{T}}(\mathbf{R} + \mathbf{H}\mathbf{B}\mathbf{H}^{\mathrm{T}})^{-1}\mathbf{H}\right). \tag{7}$$

It is always lower or equal to the total number d of observations: $0 \leq \mathscr{I}_{\mathrm{DFS}} \leq d$.

As explained earlier, it is difficult to specify **R** and **B**, especially in the retrieval of sources in atmospheric dispersion. Besides these matrices are context-dependent. In the absence of significant correlations in-between observation errors, and in-between background errors, they can be both chosen proportional to the identity matrix: $\mathbf{R} = \chi^2\mathbf{I}_d$ and $\mathbf{B} = m^2\mathbf{I}_N$. Yet, χ and especially m still need to be estimated. However, in this article, we are not interested in the precise values of χ and m. We are more interested in the degrees of freedom for the signal available for the inversion. They depend on the ratio χ/m as can be checked on Eq. (7). To some extent, reasoning in terms of DFS circumvents the necessity to reason on **R** and **B**.

Using the results of inverse modelling of actual dispersion problems: ETEX, Chernobyl, Algeciras, or from the results of carbon dioxide inverse modelling (Krysta and Bocquet, 2007; Krysta et al., 2008; Wu et al., 2011), we have found that the DFS usually represents 5%–15% of the total number of observation, for this kind of dispersion problem. In the following of this paper, rather than specifying χ, m, or the ratio χ/m, we shall assume that when dealing with real observations, one should expect to reach a DFS of about 10% of the total number of observations. In the future, with the reduction of model errors, this fraction of the DFS may increase. However a strong reduction of the model or representativeness errors may not necessarily lead to a strong increase of the ratio $\rho = \mathrm{DFS}/d$, because of the ill-posed nature of dispersion.

2.3. Multiscale data assimilation

One usually considers a regular mesh, with grid-cells of constant size in one system of coordinates, to discretise the source $\boldsymbol{\sigma}$. However, adaptive grids can also be considered to model the transport of pollutant (Constantinescu et al., 2008), or to perform source inversion (Bocquet, 2009; Bocquet et al., 2011; Bocquet and Wu, 2011). Such grids are relevant to atmospheric chemistry modelling because of the high heterogeneity of the emission fields. They are especially relevant in data assimilation for atmospheric dispersion when the observations are sparse, because the (adjoint) model can carry information from the observations in a very heterogeneous manner. We shall adopt such an adaptive grid formalism following the methodology developed in (Bocquet, 2009; Bocquet et al., 2011). Details can be found in these references, and we shall focus here on what is necessary to interpret the results.

The activity concentrations of the numerical transport model are defined on, or interpolated to, a regular grid, which is the finest available grid in the rest of this article. In the case of the CTBT problematic, the finest grid will be lat-lon, with $N_x = 512$ and $N_y = 256$. In particular the Jacobian **H** computed with the numerical model, or possibly its adjoint, is defined in this grid. The background error covariance matrix **B** is defined in this grid too.

One can define a restriction operator that coarse-grains a source $\boldsymbol{\sigma}$ defined in the finest grid into a coarser $\boldsymbol{\sigma}_\omega$ defined in an adaptive grid ω with grid-cells of various sizes but all assembled from grid-cells of the finest regular grid. A prolongation operator refines a coarse $\boldsymbol{\sigma}_\omega$ defined in the adaptive grid ω into a source $\boldsymbol{\sigma}$ defined in the finest regular grid. Coarse-graining a vector $\boldsymbol{\sigma}$ defined in the finest grid, then refining the result to project back to the finest grid does not give $\boldsymbol{\sigma}$ back, because information is lost in the coarse-graining. Rather, it gives

$$\boldsymbol{\sigma} \rightarrow \left(\mathbf{I}_{N_{\mathrm{fg}}} - \boldsymbol{\Pi}_\omega\right)\boldsymbol{\sigma}_b + \boldsymbol{\Pi}_\omega\boldsymbol{\sigma} \tag{8}$$

where $\boldsymbol{\Pi}_\omega$ is a projection operator that can be defined from the action of the restriction and the prolongation operators. N_{fg} is the number of grid-cells in the finest grid, so that $\mathbf{I}_{N_{\mathrm{fg}}}$ is the identify operator defined in the corresponding vector space. A Bayesian construction of the prolongation operator leads to a $\boldsymbol{\Pi}_\omega$ which is **B**–symmetric: $\boldsymbol{\Pi}_\omega\,\mathbf{B} = \mathbf{B}\,\boldsymbol{\Pi}_\omega^{\mathrm{T}}$. In the accidental context, the assumption $\boldsymbol{\sigma}_b = 0$ sets the constant term in Eq. (8) to zero. A schematic representation of the action of $\boldsymbol{\Pi}_\omega$ is drawn in Fig. 1. The errors caused only by the aggregation of grid-cells, which lead to representativeness errors in the observations, can be formally computed (Bocquet et al., 2011)

$$\boldsymbol{\epsilon}_\omega^{\mathrm{c}} = \mathbf{H}\left(\mathbf{I}_{N_{\mathrm{fg}}} - \boldsymbol{\Pi}_\omega\right)(\boldsymbol{\sigma} - \boldsymbol{\sigma}_b). \tag{9}$$

Performing inverse modelling in the finest regular grid yields the DFS given by Eq. (7). Bocquet et al. (2011) have shown that performing inverse modelling in the adaptive grid ω yields the DFS

$$\mathscr{J}_{\mathrm{DFS}}^{\omega} = \mathrm{Tr}\left(\boldsymbol{\Pi}_\omega\mathbf{B}\mathbf{H}^{\mathrm{T}}\left(\mathbf{R} + \mathbf{H}\mathbf{B}\mathbf{H}^{\mathrm{T}}\right)^{-1}\mathbf{H}\right). \tag{10}$$

This result assumes that representativeness errors, such as Eq. (9), are taken into account when changing resolution. The DFS can be used as a criterion to find the optimal adaptive grid given a fixed total number of grid-cells N. The algorithm to perform this optimisation is described in Bocquet (2009); Bocquet et al. (2011). In the context of atmospheric dispersion with ground-based pointwise observations, an optimal adaptive grid can deliver much more DFS than a regular grid with about the same number of grid-cells. The grid is usually refined close to the observation sites. It also depends on the dispersion itself and the meteorology. The size of a grid-cell offers a rigorous measure of the *resolution* defined by Rodgers (2000), that is to say the capacity to resolve a variable from the observations. As opposed to using the inverse of the diagonal entries of $\mathbf{P}_a$, this measure does not rely on any approximation. In practice, if a location is encompassed in a large (respectively small) grid-cell, little (respectively much) information will be obtained at this point from inverse modelling.

In the regime where χ/m is high (large error limit), it is clear that the objective function Eq. (10) can be approximated by the simpler

$$\mathscr{J}_{\mathrm{fisher}}^{\omega} = \mathrm{Tr}\left(\boldsymbol{\Pi}_\omega\mathbf{B}\mathbf{H}^{\mathrm{T}}\mathbf{R}^{-1}\mathbf{H}\right), \tag{11}$$

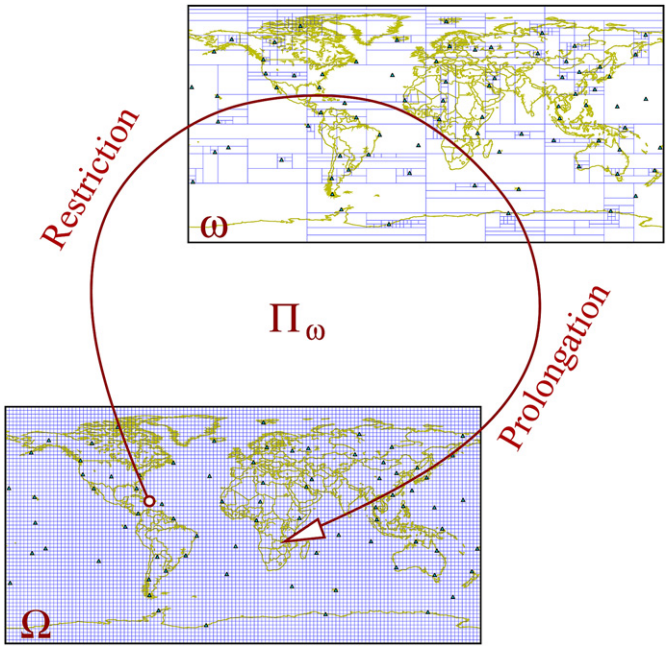

Fig. 1. Schematic for the projector $\boldsymbol{\Pi}_\omega$ which operates in the finest regular grid-cell.

called the Fisher criterion in Bocquet et al. (2011). Although the value of Eq. (11) can be different from that of Eq. (10), it was observed that the optimal grids obtained with the two criteria are very similar in the large χ/m limit.

Practically, for real applications, the ratio DFS/$d \simeq 10\%$ corresponds to a large χ/m, so that the Fisher criterion can be used in place of the DFS criterion. Moreover, in that limit it can be shown that the optimal grid is the grid that minimises the aggregation errors. Indeed, from Eq. (9), and using the $\mathbf{B}-$ symmetry of $\mathbf{\Pi}_\omega$, the aggregation error covariance matrix is

$$\mathbf{R}^{\mathrm{c}}_\omega = \mathbf{H}\left(\mathbf{I}_{N_{\mathrm{fg}}} - \mathbf{\Pi}_\omega\right)\mathbf{B}\mathbf{H}^{\mathrm{T}}. \tag{12}$$

It also characterises the representativeness errors that impact the observations as a consequence of the change of scale induced by the grid-cell aggregation. As a consequence, the normalised aggregation error can be assessed by

$$\begin{aligned}\mathrm{Tr}(\mathbf{R}^{-1}\mathbf{R}^{\mathrm{c}}_\omega) &= \mathrm{Tr}(\mathbf{R}^{-1}\mathbf{H}\mathbf{B}\mathbf{H}^{\mathrm{T}}) - \mathrm{Tr}(\mathbf{R}^{-1}\mathbf{H}\mathbf{\Pi}_\omega\mathbf{B}\mathbf{H}^{\mathrm{T}})\\ &= \mathrm{Tr}\left(\mathbf{B}\mathbf{H}^{\mathrm{T}}\mathbf{R}^{-1}\mathbf{H}\right) - \mathrm{Tr}\left(\mathbf{\Pi}_\omega\mathbf{B}\mathbf{H}^{\mathrm{T}}\mathbf{R}^{-1}\mathbf{H}\right)\\ &= \mathscr{J}_{\mathrm{fisher}} - \mathscr{J}^{\omega}_{\mathrm{fisher}}.\end{aligned} \tag{13}$$

That is why the maximisation of $\mathscr{J}^{\omega}_{\mathrm{fisher}}$ entails a minimisation of the aggregation errors.

The optimal adaptive grids that result from the optimisation of these criteria were shown to be numerically efficient to perform inverse modelling (Bocquet, 2009). They have better data assimilation performance as compared to regular grids with the same number of grid-cells. Moreover, we have just shown that they entail little aggregation errors by construction. Therefore, building such grids could be used to perform inverse modelling of IMS data. However, in the following, we shall rather focus on the fact that these grids rigorously pinpoint well observed and poorly observed regions of the world for the purpose of inverse modelling.

3. Application to the IMS radionuclide network

3.1. Setup

The potential of the global IMS radionuclide network for data assimilation with an ATM is studied in this section, using the formalism recalled in Section 2. A drastically simplified version of the setup, with unrealistic physics and annual observations, was experimented in Bocquet and Wu (2011) as a proof of concept.

Among the 80 targeted stations, 79 have assigned locations, and we shall consider these 79 stations. The year 2009 is the focus of the study. As mentioned earlier, activity concentrations measurements are integrated over 24 h. Therefore, $79 \times 365 = 28{,}835$ observations are considered. The Comprehensive Nuclear-Test-Ban Treaty Organisation has provided us with one year of influence functions (also known as sensitivities, adjoint solutions, footprints, or retroplumes), attached to each one of these observations. They correspond to the rows of the Jacobian matrix $\mathbf{H}$ built over one year. Those influence functions have been generated using the Lagrangian ATM FLEXPART (Stohl et al., 2005), version 5 (with minor modifications by the CTBTO scientists) driven by ECMWF meteorological fields at a resolution of $1^\circ \times 1^\circ$. The tracer is completely inert: only transport is considered. Hence, these influence functions represent an upper bound of how far the influence of any radionuclide can reach. The temporal extend of each influence function is 14 days, with a time step of $\Delta t = 3$ h.

Our goal is, given a fixed number of grid-cells N, to build the corresponding optimal adaptive grid for the IMS network. As explained in Bocquet (2009), the optimal grid can be chosen among a dictionary of adaptive grids. In this study, we shall choose the so-called dictionary of *tilings*: the grid-cells (*tiles*) are rectangles, and their zonal, meridional and even time lengths can be chosen independently. The adaptive grid in Fig. 1 is an example of a tiling.

With the multiscale formalism recalled earlier, it is possible to built a grid which is adaptive in space, but also in time (see the ETEX-I example of Bocquet (2009)). In this study we rather focus on a static grid, that would be optimal on average over the whole 2009 year. However, a simple average of $\mathbf{H}$ over the 365 days of the year is too naive an approach. Instead, it is necessary to average over the optimality criterion, which has a non-linear dependence in $\mathbf{H}$. In the following, we use $\mathscr{J}^{\omega}_{\mathrm{DFS}}$, or its limiting case $\mathscr{J}^{\omega}_{\mathrm{fisher}}$, where the non-linear dependence in $\mathbf{H}$ is obvious.

3.2. Daily-averaged criteria

More specifically, we look for optimal adaptive grids which are invariant by time translations of 24 h, and whose grid-cell length in time is 24 h. Therefore $\mathbf{\Pi}_\omega$ is invariant by translations of 24 h. The averaged criteria are

$$\langle\mathscr{J}^{\omega}_{\mathrm{DFS}}\rangle = \mathrm{Tr}\left(\mathbf{\Pi}_\omega\left\langle\mathbf{B}\mathbf{H}^{\mathrm{T}}\left(\mathbf{R}+\mathbf{H}\mathbf{B}\mathbf{H}^{\mathrm{T}}\right)^{-1}\mathbf{H}\right\rangle\right), \tag{14}$$

$$\langle\mathscr{J}^{\omega}_{\mathrm{fisher}}\rangle = \mathrm{Tr}\left(\mathbf{\Pi}_\omega\left\langle\mathbf{B}\mathbf{H}^{\mathrm{T}}\mathbf{R}^{-1}\mathbf{H}\right\rangle\right). \tag{15}$$

The brackets $<\cdot>$ represent the average over the 365 days of year 2009. For each one of the 365 contributions to the mean, one should identify the influence functions present in $\mathbf{H}$ that contribute to $\mathbf{B}\mathbf{H}^{\mathrm{T}}(\mathbf{R}+\mathbf{H}\mathbf{B}\mathbf{H}^{\mathrm{T}})^{-1}\mathbf{H}$, or $\mathbf{B}\mathbf{H}^{\mathrm{T}}\mathbf{R}^{-1}\mathbf{H}$. For each day t of the year, a source variable defined in a grid-cell can be causally connected through data assimilation to any of the 79 stations. However, it is causally connected to only 14 observations, at day $t+\tau$, with $\tau = 0,\ldots,13$, per station, through 14, 14-day long, influence functions.

Hence, for a given day, the number of observations that are used in the computation of $\mathbf{B}\mathbf{H}^{\mathrm{T}}(\mathbf{R}+\mathbf{H}\mathbf{B}\mathbf{H}^{\mathrm{T}})^{-1}\mathbf{H}$, or $\mathbf{H}^{\mathrm{T}}\mathbf{R}^{-1}\mathbf{H}$, is $d = 14 \times 79 = 1106$. Then, the resulting matrices are averaged over the 365 days to obtain the criterion value: $\langle\mathscr{J}^{\omega}_{\mathrm{DFS}}\rangle$, and $\langle\mathscr{J}^{\omega}_{\mathrm{fisher}}\rangle$. The numerical parallelised computation of the this average matrix demands a 3-day run on a 12-core Intel Xeon machine. For the DFS criterion, $d = 1106$ represents the maximum possible DFS, since the DFS criterion is now averaged over 365 days. In the rest of the article, these averaged criteria $\langle\mathscr{J}^{\omega}_{\mathrm{DFS}}\rangle$, or $\langle\mathscr{J}^{\omega}_{\mathrm{fisher}}\rangle$ are used to determine time-invariant optimal adaptive grids.

3.3. Dependence of the DFS in the number of grid-cells

Each optimisation is performed at a given number of grid-cells N. Fig. 2 shows the performance of the adaptive grids as compared to the regular grids at different resolution. The DFS criterion and the Fisher criterion are plotted as a function of the number N of tiles in the grid.

As mentioned in Section 2, we assume $\mathbf{R} = \chi^2\mathbf{I}_d$ and $\mathbf{B} = m^2\mathbf{I}_N$. Choosing a priori particular values for χ and m is difficult, and maybe even methodologically wrong since it was shown in Davoine and Bocquet (2007) that m should be determined a posteriori in such an accidental context. Instead, we choose the values of χ/m so as to match a given $\rho = \mathrm{DFS}/d$ ratio, which is more universal than the precise value of χ/m. In Fig. 2(b), we consider the cases where $\rho \simeq 10\%$, which is a good indication of the capability of current inverse modelling systems in the accidental context with ground point-wise observations. In Fig. 2(c), we consider the case $\rho \simeq 90\%$, as an indication for distant future systems with very low errors

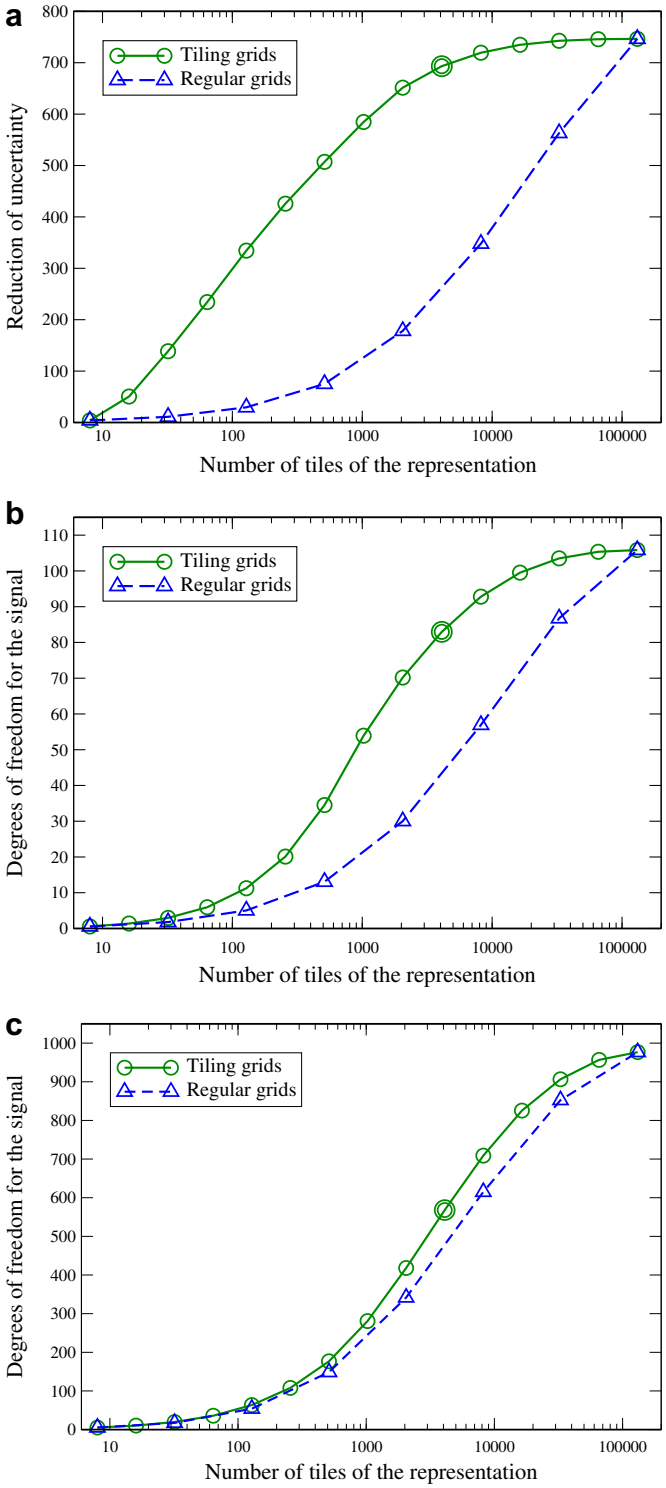

Fig. 2. Fisher criterion (a), and degrees of freedom for the signal (b, c) of optimal tilings and regular grids against the number of grid-cells in the representation. Upper panel (a): χ/m is arbitrary (just a multiplicative factor). Middle panel (b): with $\chi/m = 100$. Lower panel (c): with $\chi/m = 1$. The illustrations of Fig. 3 correspond to the points indicated by double circles.

(typically an error standard deviation 100 times smaller than in the current systems). Finally, in Fig. 2(a), we consider the limiting Fisher criterion case which corresponds to small ρ. This small ρ and conservative limit may be preferable, if one believes $\rho = 10\%$ is still too optimistic an assumption. As shown by Fig. 2, the gap between the optimal grid and a regular grid having the same number of grid-cells is increasing with the errors (instrumental, representativeness and model errors). This gives away an increase of heterogeneity of retrievals with the errors: information cannot propagate far from the network and help resolve source variables.

The fact that the curves in Fig. 2 are monotonically increasing functions of N has been proven in Bocquet et al. (2011). However future complex inverse modelling experiments will deal with scale-dependent model error, or with models operating at different scales (Lagrangian at mesoscale and Eulerian at global scale, e.g. Rigby et al. (2011)). As a consequence the general scale-dependent error decomposes into

$$\boldsymbol{\epsilon}_\omega = \boldsymbol{\epsilon} + \boldsymbol{\epsilon}^{\mathrm{c}}_\omega + \boldsymbol{\epsilon}^{\mathrm{m}}_\omega, \tag{16}$$

where $\boldsymbol{\epsilon}$ is the instrumental observational error, or any unresolved error from scales and processes defined at scales smaller than the finest grid, $\boldsymbol{\epsilon}^{\mathrm{c}}_\omega$ is the scale-covariant representativeness error determined by Eq. (12), and $\boldsymbol{\epsilon}^{\mathrm{m}}_\omega$ stands for the (possibly scale-dependant) model error. In the absence of bias and when these errors are uncorrelated, the total error covariance matrix

$$\mathbf{R}_\omega = \mathbf{R} + \mathbf{R}^{\mathrm{c}}_\omega + \mathbf{R}^{\mathrm{m}}_\omega, \tag{17}$$

needs to be accounted for in the computation of the DFS. In that case, it is expected (Peylin et al., 2001; Bocquet et al., 2011) that a maximum DFS be reached which does not correspond to the finest regular grid.

In the following, the study is performed at finite N, i.e. a computationally affordable number of grid-cells $N \ll N_{\mathrm{fg}}$, where N_{fg} is the number of grid-cells in the finest grid. Besides, the qualitative results (interpretation of the adaptive grids) will essentially be insensitive to the choice of N provided $N_{\mathrm{cg}} \ll N \ll N_{\mathrm{fg}}$, where N_{cg} is the number of grid-cells in the coarsest regular grid ($N_{\mathrm{cg}} = 8$, and $N_{\mathrm{fg}} = 131{,}072$ in this study).

3.4. Interpretation of optimal grids

Typical optimal grids are displayed for $N = 4096$ in Fig. 3. Firstly, let us consider the optimal grid based on the Fisher criterion. As explained earlier, it is impacted by the monitoring network distribution: the mesh is refined close to the stations indicating the ability of the data assimilation system to better resolve the source variables in these areas. It is also impacted by the meteorological climatology. For instance, in the polar regions, the information remains confined within the polar cells. As a result, stations in Antarctica do not significantly help in resolving variables over the Antarctic Ocean. In this high-error limit, the mesh is especially dense close to the observations: the information cannot propagate far from the stations.

Next, consider the *realistic* case where $\mathrm{DFS}/d \simeq 10\%$. Again, the grid is refined close to the observations site, but to a lesser extent. The impact of the trade winds is clear. Information is back-propagated from the tropical stations south-easterly in the South hemisphere, and north-easterly in the North hemisphere. Besides, since those winds are very directive, information cannot substantially reach the inter-tropical zone.

Finally, consider the case where model and representativeness errors are very small. The information can back-propagate much farther than in the previous cases. In particular, in the mid-latitude regions westerlies winds (maybe jets) efficiently back-propagate the information, so that the mesh is relatively even in these regions. In the tropics, the impact of the trade winds is even more obvious. Tropical regions that are not under direct observation are poorly resolved by inverse modelling.

In moderately large wind conditions, sea and land breezes may have an influence on the local climatological winds, near the

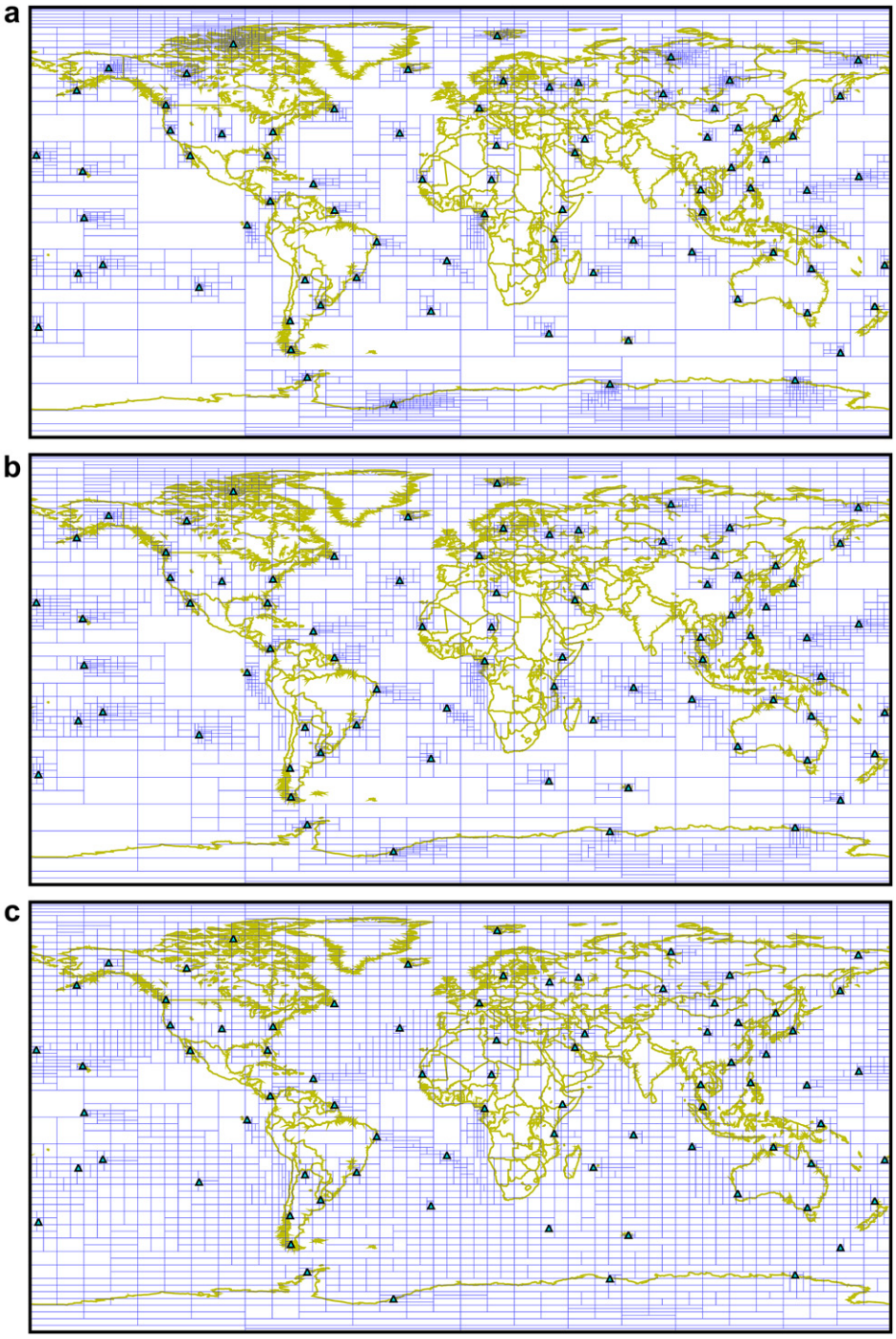

Fig. 3. Optimal adaptive grids for $N = 4096$ grid-cells. Upper panel (a): from the Fisher criterion optimisation, (b): from the DFS optimisation in the realistic case $\chi/m = 100$. Lower panel (c): from the DFS optimisation with little error $\chi/m = 1$. The stations of the IMS radionuclide network are indicated by triangles.

shores. A clear impact on the optimal grids is the poor observability of Africa, even though 6 stations are installed on the continent. Besides, the Harmattan, which is a trade wind, leaves station RN13, Edea, Cameroon, with a poor visibility on the continent. In general, for stations well inside the continent the impact of an observation station is more isotropic, but also more short-ranged.

3.5. Distribution of the DFS over the hemispheres and seasons

The degrees of freedom for the signal can be computed locally in the source space. To compute the DFS attached to a subset of source

Table 1
Distribution of the DFS over the northern (NH) and southern (SH) hemispheres and seasons.

DFS	Whole year 2009	Mar–Apr –May	Jun–Jul –Aug	Sep–Oct –Nov	Dec–Jan –Feb
NH	66.79	62.4	64.50	67.15	73.10
SH	39.06	41.49	33.75	35.88	45.23
Total	105.9	104.03	98.25	103.02	118.33

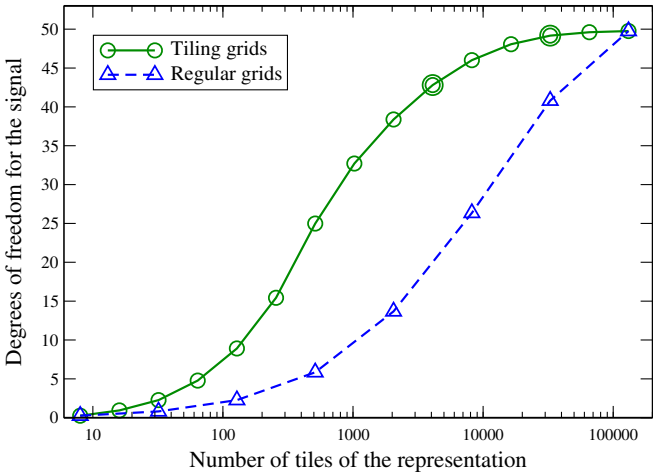

Fig. 4. Degrees of freedom for the signal of optimal tilings and regular grids against the number of grid-cells in the representation, in the case of the noble gas subnetwork ($\chi/m = 100$). The illustrations of Fig. 5 correspond to the points indicated by double circles.

variables, it suffices to compute the corresponding subtrace in the DFS formula Eq. (7), that is to say a partial sum of the diagonal entries. We have computed the DFS for the northern and the southern hemispheres, as well as for the seasons, as defined by the four trimesters March–April–May, June–July–August, September–October–November, December–January–February. Because the length of these periods can slightly vary, their DFS are given as a mean and are therefore comparable. The results are reported in Table 1. On average, the DFS of the northern hemisphere captures about 63% of the total DFS, which is consistent with the fact that 48 stations out of 79 are in the northern hemisphere. Because of this unbalance, some seasonal effects become evident. Indeed the northern hemisphere winter shows a stronger DFS than in the summer. This might be explained by the stronger westerlies winds in the winter, that propagate tracers (and related information) more remotely, in contrast to a more diffusive and less advective summer wind climatology.

3.6. Implication on the design of the network

Obviously this analysis has implications on the design of the network. The IMS radionuclide network has been evaluated and perhaps designed using detectability criteria (Wotawa et al., 2010). In the same context, other criteria could be based on the ability to map activity concentrations using the data available from the network and geostatistical techniques (Abida et al., 2008). Our criteria are based on the ability of data assimilation to retrieve source parameters. As we pointed out, it is dependent on the instrumental error, on the representativeness errors, and especially on the modelling errors. However in all circumstances, some constant features have emerged and could help in the reallocation of stations.

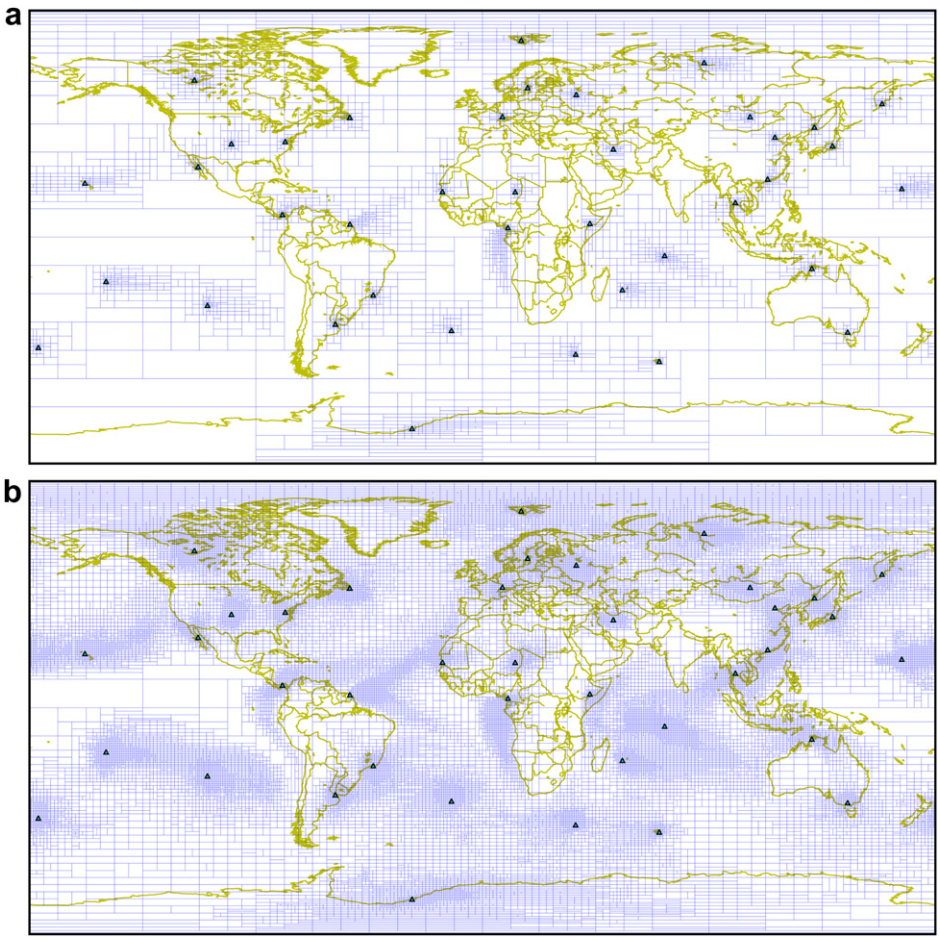

Fig. 5. Optimal adaptive grids for the 39-station noble gas network, for (a): $N = 4096$ and (b): 32768 grid-cells, using $\chi/m = 100$. The 39 stations of the noble gas network are indicated by triangles.

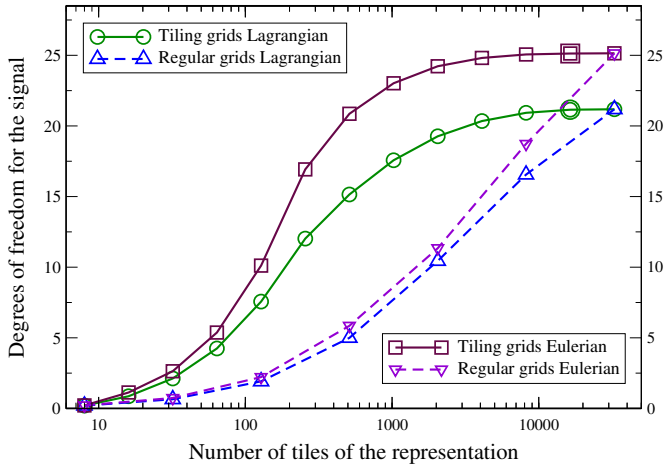

Fig. 6. Degrees of freedom for the signal of optimal tilings and regular grids against the number of grid-cells in the representation, in the case of the limited area models ($\chi/m = 100$). The illustrations of Fig. 7 correspond to the points emphasised by a double circle and a double square.

3.7. Noble gas network

We shall perform the same study but with the noble gas network which is a subnetwork of the IMS network, as stated in the treaty. Among the future noble gas 40 stations, 39 stations have a designated location, while the 40th will be the currently unknown 35th station of the 80-station radionuclide network. That is why we have chosen to perform the adaptive grid optimisation on this subset of 39 stations. The list of the stations can be found on the CTBTO website (http://www.ctbto.org) and are displayed in an interactive map (http://www.ctbto.org/map). Moreover, it is assumed that the measurement length are 24-h long, while 12-h long measurements are also performed for noble gases.

We assume the same χ/m ratio as for the realistic case of the full IMS network. The total number of observations is now $39 \times 365 = 14{,}235$. It leads to a similar ratio $\rho = \mathrm{DFS}/d \simeq 10\%$.

The behaviour of the DFS as a function of the number of grid-cells is plotted in Fig. 4. Even though it should represent a similar case to Fig. 2(b), the shape of the DFS curve stands in between the Fig. 2(a) and Fig. 2(b) cases. The fact that only 39 stations are exploited makes the globe significantly less observable by inverse

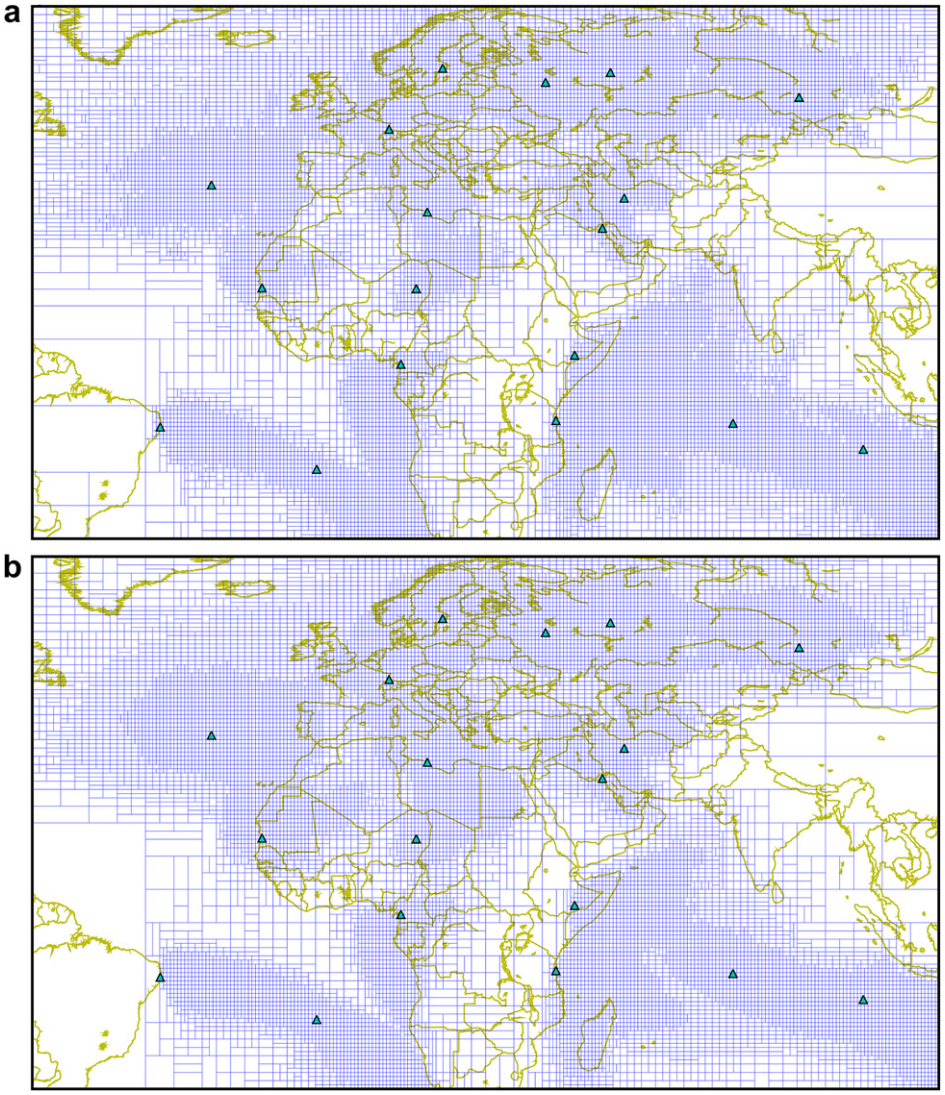

Fig. 7. Optimal adaptive grids in the limited area domain with $N = 16384$ grid-cells, computed from a Jacobian matrix **H** obtained from the influence function of (a): a Lagrangian model and (b): a Eulerian model, using $\chi/m = 100$. Within this domain only 18 stations away from the borders are considered. This helps to avoid re-entries of tracer in the Eulerian case.

modelling means. The information from the observations cannot reach remote areas, and this translates into a more rounded DFS curve, which makes optimal designed grids much more efficient than regular grid with the same number of grid-cells.

The optimal tilings for $N = 4096$ and $N = 32768$ are drawn in Fig. 5. The former allows a comparison with the full network case. The latter grid has a graphical interest since it underlies the poorly observed regions of the globe (clear/dark regions). In particular it is clear that the Pacific and the Intertropical Convergence Zone are much less observed than with the full network. In the projection chosen for Fig. 5, the apparent size of large cells covering high latitude regions should not be overrated due to the meridian convergence towards the poles. Specifically, the large cell over Antarctica has an area about three times smaller than the area of one of the two large grid-cells over the tropical Pacific.

3.8. Eulerian and Lagrangian models

As a final experiment, the inverse modelling potential of the IMS network was investigated in a limited area domain (spanning [59° W–109° E] × [29° S–69° N]), using a Lagrangian ATM (FLEXPART as used by the CTBTO), and a regional Eulerian ATM (Polyphemus/Polair3D, Quélo et al. (2007)). The limited area domain allowed us to use the regional model Polair3D, but it also allowed to significantly reduce the computational cost, since only 18 stations of the IMS radionuclide network are considered in this domain. The influence functions obtained from both models over the year 2009 simulate an atmospheric inert tracer (such as xenon-133 but without decay). The magnitude of the errors chosen for the experiment corresponds to the realistic case, where DFS/$d \simeq 10\%$. The maximal DFS (finest grid) for the Lagrangian model is about 21, while the maximal DFS for the Eulerian model is about 25. In the present context, the comparison of these two numbers should not be interpreted as a measure of the respective merit of two inverse modelling systems. Indeed, each model should in principle be endowed with its own magnitude of model errors in **R**. However, a qualitative comparison can be made with the assumption that they both carry the same errors. The DFS curves of the two systems are plotted in Fig. 6. A difference between the two types of simulation, is that since the Lagrangian influence function are computed from the global footprints, they have re-entries of tracer within the domain. To minimise the differential impact of re-entries, only 18 stations in the domain, those within an angular distance of 10° away from the boundaries, have been kept. We have checked that, on average, these re-entries do not impact the following quantitative results.

There are differences between the two sets of curves. As the number of grid-cells N increases, the DFS of the Eulerian inverse modelling system increases more than those of the Lagrangian system. With the same **R** matrix, it does not imply that one system is better than the other, but that the physics of dispersion (of the tracer and the information) is somehow different. It shows that for a same N, the Eulerian grid is more heterogeneous than the Lagrangian grid. This means that, in the Eulerian case, the tracer extends less, leading to denser influence functions around the stations. A possible explanation is that the Eulerian approach is less accurate to resolve sub-grid scale sensitivity due to, for instance, its additional implicit numerical diffusion. This is confirmed by Fig. 7 where optimal grids with $N = 16384$ were chosen because it emphasises by contrast the poorly observed areas. It clearly shows that the Lagrangian grid is less dense around the stations and extend farther. But it also gives away sampling issues for the Lagrangian grid. By comparison of the two optimal grids, it is clear that the Eulerian grid is more converged than the Lagrangian grid. We believe this is due to the fact that with 560×10^3 particles, a Lagrangian influence function may sample very well branches of the plume (better than the Eulerian model would do), but misses other possible branches of the plume. Hence, on the one hand, the Lagrangian inverse modelling system (with a limited number of particles) may capture information better than the Eulerian system does. Yet, insufficient number of particles can make the Lagrangian model suffer from the undersampling issue. This can be mitigated by empirical tests to include more particles for Lagrangian simulations (extended computational load though).

4. Conclusion

The potential of the International Monitoring System (IMS) radionuclide network has been evaluated for the inverse modelling of radionuclide releases: e.g. a nuclear explosion test or nuclear accidents like Chernobyl or Fukushima Daiichi, or the inverse modelling of the diffuse sources of xenon radio-isotopes. We have proposed an evaluation methodology accounting for the performance of the inversion (or data assimilation) system. This methodology differs from the detection capability approach and the geostatistics approach in that: i) the degrees of freedom for the signal (DFS) is chosen to be the criterion that assesses the information gain from the observations to the whole domain through inversion; ii) optimal multiscale adaptive grids of sources are constructed by maximising the DFS criterion; and iii) the radionuclide network is evaluated by the spatial distribution of the grid-cells of the optimal adaptive grids.

For optimal grids, the inverse of the size of a grid-cell measures the resolution defined as the capacity to locally resolve the source by the inversion system. Therefore the dense mesh indicates the regions where the source variables are well resolved. By contrast, for sparse mesh, the over-aggregations of the regular grid-cells at finer scale result in high uncertainties of inverted sources. Note that one type (Fisher criterion) of optimal grids yields grids with the least aggregation errors, or correspondingly to the least representativeness errors in the assimilated observations.

We have constructed global optimal grids with the IMS radionuclide network for its evaluation. The influence functions, which relate the observations with the sources, were generated using the Lagrangian transport model FLEXPART driven by ECMWF meteorological fields at a resolution of $1° \times 1°$ over the 365 days of year 2009. The ratio ρ between the DFS and the total number of observations was used to control different error levels in the inversion, i.e. the error of a priori sources and the observational error that encapsulates the instrumental error, the representativeness error and the transport model error.

Grid optimisations have been performed for three cases with $\rho \simeq 0$ (very large observational error), $\rho \simeq 10\%$ (realistic observational error), and $\rho \simeq 90\%$ (accurate transport) respectively. Some stable spatial patterns have emerged in the optimal grids with these different settings. In all cases, the trade winds carry information towards the Intertropical Convergence Zone along straight paths, leaving large unobserved areas in the tropics. For the case of large observational errors, the optimal grid is very heterogeneous. The mesh is dense close to most observation sites. The information propagation is not obvious except for the polar areas due to the impact of the polar vortices. For realistic observational errors, there are still many areas away from the information propagation path, e.g. the African continent.

When accurate atmospheric transport representation is assumed, the optimal grids become more uniformly distributed, especially for the mid-latitude regions where westerlies winds prevail. Such coverage is desirable. However, we do not believe current state-of-the-art ATM can reach that accuracy level. Moreover, even with high accuracy and a good coverage of the globe on average, the tropics will remain difficult to probe with inverse modelling.

The results obtained in this study can also serve as a basis for reallocation or installation of stations using the size of the adaptive grid-cells as an indication. It would be interesting to compare the results of this approach with the results based on the detectability criterion.

Acknowledgements

This paper is a contribution to the MSDAG project supported by the *Agence Nationale de la Recherche*, grant ANR-08-SYSC-014. The authors thank Christian Seigneur and Chris Snyder for useful discussions on the interpretation of the results. They thank John Coyne at CTBTO for a careful reading of the manuscript and his suggestions. They are grateful to an anonymous reviewer for helpful and very constructive remarks. The authors acknowledge the help of Yves Grillon and Thierry Héritier at CEA/DAM with the CTBTO/IDC source-receptor relationship files transfer. The views expressed in this paper are those of the authors and do not necessarily reflect the views of the CTBTO Preparatory Commission.

References

Abida, R., Bocquet, M., 2009. Targeting of observations for accidental atmospheric release monitoring. Atmos. Env. 43, 6312–6327.

Abida, R., Bocquet, M., Vercauteren, N., Isnard, O., 2008. Design of a monitoring network over France in case of a radiological accidental release. Atmos. Env. 42, 5205–5219.

Becker, A., Wotawa, G., Ringbom, A., Saey, P., 2010. Backtracking of noble gas measurements taken in the aftermath of the announced October 2006 event in North Korea by means of PTS methods in nuclear source estimation and reconstruction. Pure Appl. Geophys. 167, 581–599.

Bocquet, M., 2005a. Reconstruction of an atmospheric tracer source using the principle of maximum entropy. I: Theory. Q. J. Roy. Meteor. Soc. 131, 2191–2208.

Bocquet, M., 2005b. Reconstruction of an atmospheric tracer source using the principle of maximum entropy. II: Applications. Q. J. Roy. Meteor. Soc. 131, 2209–2223.

Bocquet, M., 2007. High resolution reconstruction of a tracer dispersion event. Q. J. Roy. Meteor. Soc. 133, 1013–1026.

Bocquet, M., 2009. Towards optimal choices of control space representation for geophysical data assimilation. Mon. Wea. Rev. 137, 2331–2348.

Bocquet, M., Parameter field estimation for atmospheric dispersion: application to the Chernobyl accident using 4D-Var. Q. J. Roy. Meteor. Soc., in press.

Bocquet, M., Pires, C.A., Wu, L., 2010. Beyond Gaussian statistical modeling in geophysical data assimilation. Mon. Wea. Rev. 138, 2997–3023.

Bocquet, M., Wu, L., 2011. Bayesian design of control space for optimal assimilation of observations. II: Asymptotics solution. Q. J. Roy. Meteor. Soc. 137, 1357–1368.

Bocquet, M., Wu, L., Chevallier, F., 2011. Bayesian design of control space for optimal assimilation of observations. I: Consistent multiscale formalism. Q. J. Roy. Meteor. Soc. 137, 1340–1356.

Constantinescu, E.M., Sandu, A., Carmichael, G.R., 2008. Modeling atmospheric chemistry and transport with dynamic adaptive resolution. Comput. Geosci. 12 (2), 133–151.

Davoine, X., Bocquet, M., 2007. Inverse modelling-based reconstruction of the Chernobyl source term available for long-range transport. Atmos. Chem. Phys. 7, 1549–1564.

Delle Monache, L., Lundquist, J.K., Kosovic, B., Johannesson, G., Dyer, K.M., Aines, R.D., Chow, F.K., Belles, R.D., Hanley, W.G., Larsen, S.C., Loosmore, G.A., Nitao, J.J., Sugiyama, G.A., Vogt, P.J., 2008. Bayesian inference and Markov chain Monte Carlo sampling to reconstruct a contaminant source on a continental scale. J. Appl. Meteorol. Climatol. 47, 2600–2613.

Hansen, P.C., 2010. Discrete Inverse Problems: Insight and Algorithms. SIAM.

Hourdin, F., Issartel, J.-P., 2000. Sub-surface nuclear tests monitoring through the ctbt xenon network. Geophys. Res. Lett. 27, 2245–2248.

Issartel, J.-P., Baverel, J., 2003. Inverse transport for the verification of the comprehensive nuclear test ban treaty. Atmos. Chem. Phys. 3, 475–486.

Krysta, M., Bocquet, M., 2007. Source reconstruction of an accidental radionuclide release at European scale. Q. J. Roy. Meteor. Soc. 133, 529–544.

Krysta, M., Bocquet, M., Brandt, J., 2008. Probing ETEX-II data set with inverse modelling. Atmos. Chem. Phys. 8, 3963–3971.

Nodop, K., Connolly, R., Girardi, F., 1998. The field campaigns of the European tracer experiment (ETEX): overview and results. Atmos. Env. 32, 4095–4108.

Peylin, P., Bousquet, P., Ciais, P., 2001. Inverse modeling of atmospheric carbon dioxid fluxes – response. Science 294, pp. 2292–2292.

Politis, K., Robertson, L., 2004. Bayesian updating of atmospheric dispersion after a nuclear accident. Appl. Statist. 53, 583–600.

Pudykiewicz, J.A., 1998. Application of adjoint transport tracer equations for evaluating source parameters. Atmos. Env. 32, 3039–3050.

Quélo, D., Krysta, M., Bocquet, M., Isnard, O., Minier, Y., Sportisse, B., 2007. Validation of the polyphemus platform on the ETEX, Chernobyl and Algeciras cases. Atmos. Env. 41, 5300–5315.

Rigby, M., Manning, A.J., Prinn, R.G., 2011. Inversion of long-lived trace gas emissions using combined Eulerian and Lagrangian chemical transport models. Atmos. Chem. Phys. 11, 9887–9898.

Ringbom, A., Miley, H., 2009. Radionuclide Monitoring. Science for Security: Verifying the Comprehensive Nuclear-Test-Ban Treaty. Preparatory Commission for the Comprehensive Nuclear-Test-Ban Treaty Organization, Vienna, Austria. 23–28.

Robertson, L., Langner, J., 1998. Source function estimate by means of adjoint variational data assimilation applied to the ETEX-I tracer experiment. Atmos. Env. 32 (24), 4219–4225.

Rodgers, C.D., 2000. Inverse Methods for Atmospheric Sounding. In: World Scientific, Series on Atmospheric, Oceanic and Planetary Physics, Vol. 2.

Saey, P.R.J., Bean, M., Becker, A., Coyne, J., d'Amours, R., De Geer, L.-E., Hogue, R., Stocki, T.J., Ungar, R.K., Wotawa, G., 2007. A long distance measurement of radioxenon in Yellowknife, Canada, in late October 2006. Geophys. Res. Lett. 34, L20802.

Saide, P., Bocquet, M., Osses, A., Gallardo, L., 2011. Constraining surface emissions of air pollutants using inverse modeling: method intercomparison and a new two-step multiscale approach. Tellus B 63, 360–370.

Seibert, P., Stohl, A., 2000. Inverse modelling of the ETEX-1 release with a Lagrangian particle model. In: Proceedings of the Third GLOREAM Workshop, September 1999, Ischia, Italy.

Stohl, A., Forster, C., Frank, A., Seibert, P., Wotawa, G., 2005. Technical note: the lagrangian particle dispersion model FLEXPART version 6.2. Atmos. Chem. Phys. 5, 2461–2474.

Stohl, A., Seibert, P., Wotawa, G., Arnold, D., Burkhart, J.F., Eckhardt, S., Vargas, A., Yasunari, T.J., 2011. Xenon-133 and caesium-137 releases into the atmosphere from the Fukushima Dai-ichi nuclear power plant: determination of the source term, atmospheric dispersion. Atmos. Chem. Phys. Discuss. 11, 28319–28394.

United Nations, 1996. Protocol of the Comprehensive Nuclear-Test-Ban Treaty. Preparatory Commission for the Comprehensive Nuclear-Test-Ban Treaty Organization, Vienna, Austria.

United Nations, 2000. United Nations: Sources and Effects of Ionizing Radiation. United Nations Scientific Commitee on the Effects of Atomic Radiation. Report to general assembly. Tech. rep., United Nations, New-York.

Vogel, C.R., 2002. Computational Methods for Inverse Problems. SIAM. Frontiers in Applied Mathematics.

Winiarek, V., Bocquet, M., Saunier, O., Mathieu, A., 2012. Estimation of errors in the inverse modeling of accidental release of atmospheric pollutant: application to the reconstruction of the cesium-137 and iodine-131 source terms from the Fukushima Daiichi power plant. J. Geophys. Res. 117, D05122. doi:10.1029/2011JD016932.

Winiarek, V., Vira, J., Bocquet, M., Sofiev, M., Saunier, O., 2011. Towards the operational estimation of a radiological plume using data assimilation after a radiological accidental atmospheric release. Atmos. Env. 45, 2944–2955.

Wotawa, G., Becker, B., Kalinowski, M., Saey, P., Tuma, M., Zahringer, M., 2010. Computation and analysis of the global distribution of the radioxenon isotope Xe based on emissions from nuclear power plants and radioisotope production facilities and its relevance for the verification of the Nuclear-Test-Ban Treaty. Pure Appl. Geophys. 167, 541–557.

Wotawa, G., De Geer, L.-E., Denier, P., Kalinowski, M., Toivonen, H., D'Amours, R., Desiato, F., Issartel, J.-P., Langer, M., Seibert, P., Frank, A., Sloan, C., Yamazawa, H., 2003. Atmospheric transport modelling in support of CTBT verification–overview and basic concepts. Atmos. Env. 37, 2529–2537.

Wu, L., Bocquet, M., 2011. Optimal redistribution of the background ozone monitoring stations over France. Atmos. Env. 45, 772–783.

Wu, L., Bocquet, M., Lauvaux, T., Chevallier, F., Rayner, P., Davis, K., 2011. Optimal representation of source-sink fluxes for mesoscale carbon dioxide inversion with synthetic data. J. Geophys. Res. 116, D21304.

Yee, E., Lien, F.-S., Keats, A., D'Amours, R., 2008. Bayesian inversion of concentration data: source reconstruction in the adjoint representation of atmospheric diffusion. J. Wind Eng. Ind. Aerodynamics 96, 1805–1816.